# Assessment of direct image processing methods to measure the apparent contact angle of liquid drops

D. Biolè[1], M. Wang[2], V. Bertola[1*]

[1]School of Engineering, University of Liverpool, Brownlow Hill, Liverpool, L69 3GH, UK

[2]Department of Engineering Mechanics and CNMM, Tsinghua University, Beijing 100084, China

*e-mail: Volfango.Bertola@liverpool.ac.uk

## Abstract

Four methods to measure apparent contact angles of non-axisymmetric drops are analysed critically. In particular, methods based on local edge interpolation or fitting are compared with direct image processing methods, based on image filtering with a suitable sampling mask. The methods performance is evaluated based on the dynamic contact angle of a dilute polymer solution drop impacting on a solid substrate. Results show that direct image processing methods yield an overall better performance, with a good compromise between measurement accuracy and computational cost, and have a limited dependence on the choice of parameters. Polynomial edge fitting yields the worst performance, both in terms of accuracy and in terms of computational cost.

# 1. Introduction

The contact angle of a drop deposited on a solid surface, defined as the angle between the solid surface and liquid–air interface on the side of the liquid phase, is probably the most important quantity of surface science, which is used to characterise the wettability of solid surfaces [1-4], drop condensation or evaporation [5,6], icing [7,8], drop impact phenomena [9,10], adhesion between drops and solid surfaces, and many other practical applications [11-13]. For this reason, an accurate measurement of the contact angle is of fundamental importance not only for the purpose of scientific research, but also in a wide range of practical applications. Existing contact angle measurement techniques rely either on the measurement of the liquid-solid interaction force, and relate it to the contact angle through the Young-Laplace equation [14,15], or on the direct measurement of the contact angle using optical methods, generally on a liquid drop in contact with a solid surface [16]. It important to remark that the problems of contact angle definition, measurement and analysis are far from being well understood to date, and they are intensely debated in the recent literature [17-20].

Methods based on force tensiometry provide the value of the intrinsic contact angle in the case of pure fluids at thermodynamic equilibrium when the surface and interfacial tensions are known; however, in several practical circumstances the observed (or apparent) contact angle is different from the equilibrium contact angle, and optical methods are preferred. In particular, the contact angle value can be affected by impurities in the fluid [21], line tension [22,23], adsorption of the vapour onto the solid phase [24], electrostatic potential [25], surface roughness [26,27] or chemical heterogeneity [28], and external forces. Another important case where optical methods are the only option available to measure contact angles is represented by drops in non-equilibrium conditions, such as droplets moving on an inclined surface, or under the action of aerodynamic drag, and drops impacting onto solid surfaces.

In optical methods, contact angles are generally measured from the two-dimensional side view of drops placed on the solid surface; a standard approach consists in fitting one or more analytical functions to the drop shape, or to a part of it in the neighbourhood of the contact (three-phase) point. The most widely used technique to date is the Axisymmetric Drop Shape Analysis method [29-33], where a solution of the Laplace equation is fitted to the drop shape by minimising the error between the theoretical and observed drop boundaries. This method is available in several versions, some using a circle to fit the drop boundary in order to increase the processing speed [34,35]; in this case, the method is less accurate, especially when the drop size exceeds the

capillary length, i.e. when gravity dominates over surface forces, and drops do not have the shape of a spherical cap [36].

A limitation of ADSA and other similar methods is they require drop symmetry, which makes these methods not suitable for several applications, such as drops moving on an inclined surface, or drops impacting on a solid surface. In fact, during impact the drop shape undergoes large, non-symmetric deformations, and apparent contact angles cover almost the entire range between 0° and 180°, as shown in Figure 1; thus, it is almost impossible to fit with sufficient accuracy the drop shape, or even a limited part of it.

The local contact angles of non-axisymmetric drops can be calculated if the drop volume, the capillary length, and the entire contact line are know [37], however the accuracy of this method relies heavily on that of the contact line measurement, which may be affected by discretization and/or perspective errors when reconstructed from side views of the drop at different angles [38]. An alternative approach consists in fitting polynomials to find the drop boundary in a small portion of the drop edge near the contact line [39,40]. The simplest is to approximate the local tangent with a line interpolating the three-phase-point and the nearest point of intersection between the shifted baseline and the interface (i.e., to approximate the drop edge with a $1^{st}$-order polynomial). Although the separate analysis of the two edges of the drop allows one to measure contact angles in non-symmetric drops, it does not allow a prompt identification of the contact line, introducing an error whenever the baseline is not perfectly horizontal; these methods are also very sensitive to the order of the fitting polynomial and to the local image resolution, although accuracy can be improved using sub-pixel resolution [41].

A simple edge-fitting method for asymmetric drops uses piecewise continuous polynomial functions (B-splines) [42,43]; these curves can fit reasonably well any drop shape, provided suitable nodes are selected on the drop edge. However, since these optimum nodes are specified manually by the user, the method is impractical to analyse large stacks of images, for example those generated by high-speed imaging systems.

Direct image processing methods measure the contact angle without edge fitting. In particular, when the edge map of the drop is available, two alternative approaches are possible: one based on local edge contour analysis [44] and another based on image intensity gradient analysis [45]; unlike edge fitting approaches, these methods are less sensible to image resolution. It is worth mentioning that it is also possible to enhance the quality of raw digital images before the least-squares best fit [46], however this method still relies significantly on the quality of original images.

This paper presents a comparative assessment of four image-processing techniques for the contact angle measurement (the secant method, edge fitting, local contour analysis and intensity gradient analysis, respectively). All methods are used to measure contact angles on the same images, obtained from a single set of experiments as described in Section 2; Section 3 contains a mathematical description of the four image processing algorithms, while results are reported in Section 4.

## 2. Experiments and image pre-processing

### 2.1 Experiments

Different contact angle measurement algorithms were tested on side views of a liquid droplet impacting on a PTFE-coated glass slide with impact Weber number, $We = \rho u^2 D/\sigma$, where $\rho$ is the fluid density (~1000 kg/m$^3$), u the impact velocity (~1.06 m/s), D the drop diameter (~3 mm), and $\sigma$ the surface tension (~70 mN/m), equal to 48. The fluid was a 50 mg/L solution of polyethylene oxide (Aldrich Chemicals, M$_w$ = 4000 kDa, $\rho$ = 1210 kg/m$^3$) in de-ionized water.

A schematic description of the experimental setup is shown in Figure 1. A high-frame rate CMOS camera (Phantom v9000) equipped with a zoom lens (Edmund Optics VZi400) and horizontally aligned with the surface recorded the impacts of single drops. Back-to-front illumination was provided by a LED backlight, which ensured uniform illumination intensity, and images with a resolution of 576×286 pixels were captured at 8000 frames per second. Magnification was kept constant throughout all experiments and lengths on the image could be calculated by comparison with a reference length (spatial resolution: 16.26 µm/pixel). To ensure a fine optical alignment, the camera, the impact surface and the backlight were fixed to an optical breadboard.

A complete description of the experimental setup and of the experimental procedure can be found in [47].

### 2.2 Test images definition and pre-processing

Similar to most high-speed imaging data, drop impact frames captured by the CMOS camera are characterized by very low brightness and contrast [47-49]. Thus, during experiments a reference frame containing only the background of the drop with approximately the same illumination conditions was also recorded for every impact. Then, the background subtraction formula for linear detectors [45,50] was used to obtain a smoothed background and avoid aliasing in edge detection; this method was preferred to histogram equalization and image sharpening algorithms

[51,52]. As shown in Figure 2, the pre-processed drop frames were particularly clean and with an approximately uniform contrast between the captured object (i.e., the drop) and the background. The Canny edge detector [53] was used to find the air-liquid interface on each image of the stack; edge detection was performed with constant parameters for all the experimental data-set, with very low and uniform smoothing (i.e. a Gaussian mask of 7 px size and width $\sigma$ = 1.5). The output of the algorithm was an edge map, i.e. a binary matrix where only the pixels corresponding to local maxima of the image intensity gradient are equal to one.

The interface detected by Canny algorithm is displayed in Figures 3c and 3d with a black solid line drawn over pre-processed images; the position of the contact points (i.e., the drop edge), represented with white circles, was set at the intersection of the drop interface with the base line, determined previously.

# 3. Contact angle measurement

## 3.1 Secant method

The secant method probably represents the simplest among the image-processing algorithms assessed in the present paper; however, simplicity does not mean inaccuracy. In fact, if the algorithm parameters are chosen carefully, it can be a reliable method, characterized by low computational cost and high repeatability of the results.

The main concept of the secant method is to approximate the tangent to the drop interface in the contact point with a secant, i.e. a line that is simultaneously intercepting the three-phase point and another point of the interface, as shown schematically in Figure 4a. The approach is accurate if the second point of the interface is chosen close enough to the reference three-phase point on the baseline, i.e. the distance from the baseline, Δy in Figure 4a, is small; in discretised images, however, if Δy is too small the angle resolution is poor. In pixel resolution, distance minimization is unfeasible: for example, if Δy=1 angles in the range between 45° and 135° cannot be measured, with the exception of θ=90°. This is an intrinsic limit of algorithm, which can be overcome only when a sub-pixel-resolved version of the edge map (e.g. obtained by interpolation) is used, or a better resolved input image is provided. Despite this issue, the algorithm is attractive from a computational point of view because it requires only the scan of one line the edge map.

In formulae, the secant algorithm receives as input the substrate height, $y_{sub}$, and the parameter Δy, which are used to find the three-phase point and the reference point (indicated as squared dots in Figure 4a) in the edge map, hence measure $\Delta x$ and calculate the angle as:

$$\theta = arctan\left(\frac{\Delta y}{\Delta x}\right) \qquad\qquad (1)$$

## 3.2 Polynomial edge fitting

Amongst all the edge fitting algorithms one can find in literature [17], [19], [20], polynomial fitting [26], [27] represents an interesting alternative to ADSA [16] and to contact line morphology analysis [24]. This method can measure the contact angle from side views of non-axisymmetric sessile droplets, without previous characterization of the fluid and of the substrate wetting properties, and including correction of perspective errors [25].

To summarise the polynomial edge fitting method in few formulae, one can consider a finite set of N discrete points (N $\geq$ 1), with coordinates $\{x_i, y_i\}$, where i = 1,…,N, the coefficients $c_n$ of a least-squares fitting polynomial of order p (p < N) are obtained by minimizing the overall squared error; if the point coordinates are rewritten as $\{x_i, \sum_{n=0}^{p} c_n x_i^n + \varepsilon_i\}$, this function is $\varepsilon^2 = \sum_{i=1}^{N} \varepsilon_i^2$. The over-determined linear set of equations $\mathbf{y} = \mathbf{X}\,\mathbf{c} + \boldsymbol{\varepsilon}$ in the unknown vector $\mathbf{c}$, admits solution $\hat{\mathbf{c}} = \mathbf{A}^{-1}\mathbf{b}$ where $\mathbf{A} = \mathbf{X}^\mathbf{T}\mathbf{X}$ is the matrix of coefficients and $\mathbf{b} = \mathbf{X}^\mathbf{T}\mathbf{y}$ the constant terms vector. The direct manipulation of the matrix $\mathbf{A}$ and of the vector $\mathbf{b}$ can be used to force the polynomial to interpolate a specific point, i.e. $y_i = \sum_{n=0}^{p} c_n x_i^n$ (a point without error); in the case of the contact point (or three-phase point, TPP), the mixed least-squares/interpolating polynomial is obtained by substituting the first constant term $b_1$ with $y_{TPP}$ and the first row of $\mathbf{A}$ with $[1 , \ x_{TPP} , \ x_{TPP}^2 , \ \cdots , \ x_{TPP}^n]$. Once the set of equations is solved, the angle $\phi$ is calculated from the slope of the local tangent in the contact $y'_{TPP}$ as:

$$\phi = \arctan(y'_{TPP}) \approx \arctan\left(\sum_{n=1}^{p} n\hat{c}_n x_{TPP}^{n-1}\right) \qquad\qquad (2)$$

Figure 4b shows an example of 2$^{nd}$ order polynomial fitting for the same discretised edge used in Figure 4a, and the resulting tangent line in the contact point. Although the comparison of Figures 4a and 4b suggests that polynomial fitting provides more accurate contact angle measurements than the secant method, this approach is not entirely accurate under some circumstances; in particular, the selection of the edge points and the choice of the order of the polynomial are critical to achieve good accuracy. For example, if the N = 11 points of the reference geometry used in Figure 4 are fitted with polynomials of orders 2 to 4, the slope of the resulting tangents in the three-phase-point is surprisingly different, because this is the node where the largest fitting error accumulates (i.e., the end node). The same issues are not eliminated by edge map interpolation, i.e. boosting data to sub-pixel-resolution [28]. Most likely, the only advantage of this operation is a slight increase of the rank of the linear system associated to the least-squares-fit problem;

however, this is by definition larger than the number of unknowns (i.e., the problem is over-determined).

In addition to the above, specific implementations of this method may have other issues. For instance, in the code SPPF v4.3 [41,57] the contact angle is evaluated recursively by increasing the number of interface points (N) at each step, starting from the three-phase-point; the optimum set of interface points is defined as the group of nodes with the minimum sensitivity to the number of points, however this criterion does not ensure either the polynomial best fit optimization or the contact angle accuracy. Moreover, the polynomials used to fit the drop edge are not interpolating the contact point; thus, the contact angle is not measured exactly at the contact point, but in a different point shifted in the vertical direction, which introduces another error.


### 3.3 Local contour analysis

Local contour analysis algorithms are usually characterized by low performance due to the errors that can be encountered in the definition of the contour mask [51,52]; however, for the specific case of drop impact images the definition of the computational array is somewhat easy and extremely precise [44]. In fact, when the intensity of the background is subtracted from a drop image and the edge map is calculated, the binary image resulting from filling with ones the region outside the interface and with zeros the region inside it, is both representative of the object (i.e., the drop) and resolved as the interface. An example is displayed in Figure 5a for the case of a polymer solution drop with $C_{\mathrm{PEO}} = 50 \ \mathrm{mg/L}$ , impacting on a solid surface with $\mathrm{We} = 48$, 10 ms after impact.

With reference to the geometry displayed in Figure 5b, the slope of any edge point **e** (e.g. the three phase point) is correlated to the area defined by the overlap of the image and a suitable test shape, defined in matrix form according to Eq. 3:

$$M[\mathbf{i}] = \begin{cases} 1/b^2 & \text{if} \quad r \geq b \quad \text{and} \quad r - b + 1 \leq c \leq 3b - r - 1 \\ 0 & \text{otherwise} \end{cases} \tag{3}$$

This area is obtained by calculating the convolution of the image matrix $\mathbf{i} = [r,c]^T$ (where $r$ and $c$ are the row and the column number, respectively) with the test shape matrix (Eq. 3), which therefore is also called goniometric mask:

$$\alpha[\mathbf{e}] = (\mathrm{L} * \mathrm{M})[\mathbf{e}] \tag{4}$$

In Eq. (4), the vector [**e**] contains the coordinates of a given point of the contour line; in the case of the contact point, $\mathbf{e}_{TPP} = [y_{TPP}, x_{TPP}]^T$. A graphical representation of the goniometric mask is displayed in Figure 5c. In particular, the above procedure to estimate the tangent slope holds for

any triangular convolution mask with a size $m = 2b - 1$, where $b \in \mathbb{N}$ (purged from the null element). The contact angle can be then obtained from purely geometric considerations [44]:

$$\vartheta[\mathbf{e}] = \pi \frac{1 - \mathrm{sgn}\,(\lambda[\mathbf{e}])}{2} + \arctan\left(\frac{1}{\lambda[\mathbf{e}]} - \mathrm{sgn}\,(\lambda[\mathbf{e}])\right) \tag{5}$$

where

$$\lambda[\mathbf{e}] = 2\alpha[\mathbf{e}] + 1 \tag{6}$$

The quantity $b^2$ in Eq. (3) also represents the number of different angles measurable by the algorithm, hence, $\pi/b^2$ is the expected angular resolution; for example, a minimum measurable angle of one degree is obtained for $b \approx \sqrt{180} = 13.41$. The algorithm accuracy depends both on the test mask size $m$ and on the specific background image considered; in general, it increases when the image resolution is larger, however, to avoid excessive contour smoothing the mask size $m$ should be kept as small as possible [31].

## 3.4 Intensity gradient analysis

The image intensity gradient is a cost-less source of information for contact angle measurement when edge points are defined as local maxima of $\|\nabla I\| = \sqrt{I_x^2 + I_y^2}$, for example using the Canny method [45,53]. An easy way to obtain smoothed directional derivatives is to filter an image $I$ with the well-known Gaussian derivative kernels [50,52] (denoted as $g_x$ and $g_y$ in the present work):

$$I_x[\mathbf{i}] \approx G_x[\mathbf{i}] = (I * g_x)[\mathbf{i}] \tag{7}$$

$$I_y[\mathbf{i}] \approx G_y[\mathbf{i}] = (I * g_y)[\mathbf{i}] \tag{8}$$

An example of intensity gradient data is provided in Figure 5d, for the same drop image discussed in Section 3.3 above.

The concept behind this algorithm is to determine the slope of the maximum likelihood tangent line to the drop interface, using the intensity gradient as weighing function [45]. The smoothed gradient peaks in correspondence of any edge point; as discussed previously for the polynomial edge fitting, the position of these points is critical to determine the slope of the tangent to the drop edge hence the contact angle. However, edge detection may not be accurate due to excessive smoothing during the image differentiation, or to a too high hysteresis threshold; as a result, the edge map will generally contain only the information that the analyst interpreted as edge points according to some arbitrary criterion (e.g., by parameter tuning) [58,59]. When the intensity data are not segmented, i.e. edges are not of step type, the region of the intensity gradient surrounding any edge point is not null, and is shaped accordingly to the local direction of the apparent edge curve (see Figure 5d). Thus, from the computational point of view a small

sample of the local gradient intensity centred on any edge point is directly related to a probability distribution of the tangent slope [32].

In formulae, considering again a matrix size $m = 2b - 1$ as in Section 3.3, the centred directional increment masks are defined as $\Delta_x = \mathbf{1}_m \cdot \Delta_m^T$ and $\Delta_y = \Delta_m \cdot \mathbf{1}_m^T$; where $\mathbf{1}_m = [1, \cdots, 1]^T$ is the unit vector and $\Delta_m = -b + [1, 2, 3, \cdots, m]^T$ is the increment vector. Under discretization, the natural test function $\phi(x, y) = \arctan(y/x)$ must be modified to avoid ill-defined components (i.e. the core point $r = c = b$) and biasing (e.g. the average angle of a vertical line, obtained for $\phi = \pi/2$ or $\phi = -\pi/2$, is $\phi = 0$); in summary, the directional mask, a graphical representation of which is displayed in Figure 5e, is given by:

$$\Phi[\mathbf{i}] = \begin{cases} 0 & \text{if} \quad r = c = b \\ \pi/2 & \text{if} \quad c = b \quad \text{and} \quad r \neq b \\ \arctan\left(\Delta_y[\mathbf{i}]/\Delta_x[\mathbf{i}]\right) & \text{otherwise} \end{cases} \qquad (9)$$

Biasing is an intrinsic shortcoming of discretization that requires resampling the image gradient with a particular weighting function (i.e., another mask) while doing the angle measurement. In practice, the weighing mask W yields a uniform probability density of the tangent slope by shifting and normalizing the original distribution, $\text{pdf}(\Phi[\mathbf{i}]) = n(\Phi[\mathbf{i}])/N$, by its minimum and maximum values, $2/N$ and $m/N$, respectively; $n(\Phi)$ is the number of repetitions of the angle $\Phi$ in the mask and $N = m^2 - 1$ the total number of angles measurable when the mask size is $m$. In conclusion, the weighing mask takes the form:

$$W[\mathbf{i}] = \frac{\frac{1}{\text{pdf}(\Phi[\mathbf{i}])} - \frac{N}{m}}{\frac{N}{2} - \frac{N}{m}} = \frac{\frac{m}{n(\Phi[\mathbf{i}])} - 1}{\frac{m}{2} - 1} \qquad (10)$$

And the final probability distribution of the edge slope is:

$$\Phi[\mathbf{e}] = \frac{\left(\|\nabla I\| * \{W \circ \Phi\}\right)[\mathbf{e}]}{\left(\|\nabla I\| * W\right)[\mathbf{e}]} \qquad (11)$$

When the drop reflection on the substrate is also captured in the image, which is desirable to find the location of the drop baseline, the average angle value calculated by Eq. (11) is approximately zero at the contact point, therefore a further step is required. This property can be used, however, to find the three-phase-points and, if the entire droplet is visualized, to estimate the baseline inclination [32]. In the sample image of Figure 5d, for instance, the baseline inclination is $0.84°$, which is not immediately visible from image inspection.

When the bisymmetry of the masks $\Phi$ and W is broken, i.e. when only one half of the matrix is considered (see Eqs. 12 and 13), contact angle measurement is possible with Eq. (11) because the reflection of the drop on the substrate does not balance the statistic of the tangent slope, biasing it to zero.

$$\Phi^{north}[\mathbf{i}] = \begin{cases} \Phi[\mathbf{i}] & \text{if} \quad r \geq b \\ 0 & \text{otherwise} \end{cases} \tag{12}$$

$$W^{north}[\mathbf{i}] = \begin{cases} W[\mathbf{i}] & \text{if} \quad r \geq b \\ 0 & \text{otherwise} \end{cases} \tag{13}$$

The masks $\Phi^{north}$ and $W^{north}$ are graphically represented in Figures 5d and 5e, respectively, for a matrix half-size $b = 10$.


## 4. Results

### 4.1 Single image test

The four methods outlined above (secant, polynomial edge fitting, local edge analysis and the intensity gradient analysis) were initially compared with one another on the two drop images shown in Figure 3, one with contact angle < 90° and the other with contact angle > 90°, respectively; test frames were selected within the frame stack describing the impact of a 50 mg/L polymer solution drop with impact Weber number We = 48. Results are presented in Figure 6, where the method parameter b represents alternatively either the vertical distance from the baseline used for contact angle calculation in the case of the secant method, or the number of edge pixels used in polynomial edge fitting, or the mask size in the cases of local edge contour analysis and intensity gradient statistic.

Despite its simplicity, in these experiments the secant method provided good results when the distance from the baseline was larger than 10 pixels (Figures 6a, 6b and 6c); the coarse angle discretization in the range $45° \leq \vartheta \leq 135°$, due to the main shortcoming of this technique highlighted in Section 3.1, strongly affected the contact angle value in the second case (Figure 6b) when the offset distance was less than 10 pixels, as shown in Figure 6c.

In the case of the polynomial edge fitting, the tangent lines plotted in Figures 6d and 6e correspond to contact angles measured by 2nd order least-squares-fitting polynomial functions interpolating the three-phase point. In Figure 6f, these results (with label INTP) are also compared with those obtained without interpolating the three-phase point using the SPPF code [41,57] (label SPPF). In the case with θ < 90° the contact angle measured by both methods was comparable and in agreement with the results obtained using the secant method. However, in the case with θ > 90° the results obtained with the SPPF code are significantly different from those obtained with other methods.

The results obtained by local edge analysis, displayed in Figures 6g, 6h and 6i, and by intensity gradient statistics, displayed in Figures 6j, 6k and 6l, respectively appear more reliable and less

sensitive to the parameter choice in comparison with the above methods. In particular, it should be noted the quality in the tangent approximation achieved by the local contour analysis method in the case with θ >90°, where the tangent lines obtained with different mask sizes have almost exactly the same slope, as shown in Figure 6h.

Overall, the intensity gradient statistics method yields the best performance (including independence of the sampling mask size) for $b \geq 7$. The optimum size of the mask results from a trade-off between the need to capture small features or poorly resolved images (smaller mask) and angle measurement resolution (larger mask).

## 4.2 Image stack test

The methods performance in measuring the dynamic contact angle of impacting droplet was assessed on the full stack of images (about 2,400 frames) describing the drop impact process during the first 300 ms after impact. The resulting contact angles are displayed in Figure 7, where each row corresponds to a different algorithm (from top to bottom: secant, edge-fitting, local contour analysis, and intensity gradient statistic), and each column corresponds to a different value of the parameter (the offset distance, the number of nodes, and the mask size, respectively). The polynomial edge fitting algorithm (the version interpolating the contact point is considered here) exhibits the worst performance: the contact angle is clearly polarized to the value $\vartheta = 90°$ and when it is not, it exhibits high frequency oscillations (spikes). Although the former issue can be removed by switching the Cartesian coordinates (e.g. [46]), this may not be easy to do with large stacks of images and rapidly changing contact angles.

The performance of other methods is almost comparable, with differences in the range $\pm 5°$. It is interesting to note the smoothness of the data obtained by applying the local edge analysis (Figures 7g, 7h and 7i) and the intensity gradient statistics (Figures 7j, 7k and 7l) depends significantly on the mask size, while smoothness of measurements obtained with the secant method is less sensitive to the offset distance.

When processing large stacks of images, the computational cost of the method becomes important. As expected, the secant method is fasted because of its simplicity; taking this method as a reference (computational cost = 1) the computational cost of the other algorithms is approximately 20 for the local contour analysis, 50 for the intensity gradient statistics and more than 100 for the polynomial edge-fitting.

It is important to remark that, especially in the case of dynamic contact angle measurements, the assessment of different well-known techniques can be only relative to one another; in fact, there

is no absolute reference measurement to compare with, and not even a widely accepted reference method (such as the ADSA in the case of droplets in thermodynamic equilibrium). Nevertheless, the above comparative analysis demonstrates the severe limitations of the polynomial edge fitting techniques, and shows that other methods are more reliable and robust even when they are not used by a skilled operator.

# 5. Conclusions

Four methods to measure contact angles of non-axisymmetric drops (secant method [33], polynomial edge fitting [28], local contour analysis [31], and gradient intensity statistics [32]) were reviewed, and their performances assessed based on the test case of a liquid droplet impacting on a solid substrate.

Results show that direct image processing methods, which do not require edge fitting, yield better overall performances than other methods. In particular, due to its probabilistic nature, the gradient intensity statistics method returns consistently accurate results even when processing large stacks of images displaying contact angles in a wide range of values, from very small to very large; its results do not depend significantly on the parameter choice. In terms of computational cost (i.e., execution speed), the secant method ranks first, resulting 20 to 100 times faster than other methods.

Polynomial edge fitting has the overall worst performance, both in terms of accuracy and in terms of computational cost; in particular, this method is extremely sensitive to the choice of interpolation nodes, whether manual or automatic, and to choice of the coordinate system when measuring angles around 90°. A good compromise in terms of efficiency (i.e. expressed as cost-quality) is represented by the local contour analysis, which provides good results with a reasonable computational cost.

# Acknowledgments

# References

1.  P.-G. de Gennes, Wetting: statics and dynamics. Rev. Mod. Phys. 57 (1985) 827–863.

2.  R. Förch, H. Schönherr, A. Tobias, A. Jenkins, Surface design: applications in bioscience and nanotechnology. Wiley-VCH. ISBN 3-527-40789-8 (2009).

3.  J. T. Cieslinski, K. Krygier, Sessile droplet contact angle of water-$Al_2O_3$, water-$TiO_2$ and water-Cu nanofluids, Experimental Thermal and Fluid Science 59 (2014) 258-263.

4.  B. Vadgarna, D. K. Harris, Measurements of the contact angle between r134a and both aluminum and copper surfaces, Experimental Thermal and Fluid Science 31 (2007) 979-984.

5.  G. McHale, S.M. Rowan, M.I. Newton, M.K. Banerjee, Evaporation and the wetting of a low energy surface, J. Phys. Chem. B 102 (1998) 1964–1967.

6.  F. M. Mancio Reis, P. Lavieille, M.Miscevic, Toward enhancement of water vapour condensation using wettability gradient surface, Experimental Thermal and Fluid Science 67  (2015) 70-74.

7.  Z.-J. Wang, D.-J. Kwon, K. L. DeVries, J. M. Park, Frost formation and anti-icing performance of a hydrophobic coating on aluminum, Experimental Thermal and Fluid Science 60 (2015) 132-137.

8.  L. Huang, Z. Liu, Y. Liu, Y. Gou, L. Wang, Effect of contact angle on water droplet freezing process on a cold flat surface, Experimental Thermal and Fluid Science 40 (2012) 74-80.

9.  J. H. Moon, D. Y.  Kim, S. H. Lee, Spreading and receding characteristics of a non-newtonian droplet impinging on a heated surface, Experimental Thermal and Fluid Science 57 (2014) 94-101.

10. S. Sen, V. Vaikuntanathan, D. Sivakumar, Experimental investigation of biofuel drop impact on stainless steel surface, Experimental Thermal and Fluid Science 54 (2014) 38-46.

11. G. Kugel, T. Klettke, J.A. Goldberg, J. Benchimol, R.D. Perry, S. Sharma, Investigation of a new approach to measuring contact angles for hydrophilic impression materials, J. Prosthodont. 16 (2007) 84–92.

12. D. Daffonchio, J.Thaveesri, W.Verstraete, Contact angle measurement and cell hydrophobicity of granular sludge from upflow anaerobic sludge bed reactors, J. Appl. Environ. Microbiol. 61 (1995) 3676–3680.

13. F. Salaun, E. Devaux, S. Bourbigot, P. Rumeau, Application of contact angle measurement to the manufacture of textiles containing microcapsules, Textile Res. J. 79 (2009) 1202–1212.

14. J.K. Spelt, A.W. Neumann, Applied Surface Thermodynamics, Dekker, NewYork, 1996, pp. 379–412.

15. C. Della Volpe, D. Maniglio, M. Morra, S. Siboni, The determination of a 'stable-equilibrium' contact angle on heterogeneous and rough surfaces Colloids and Surfaces a-Physicochemical and Engineering Aspects 206 (2002) 47-67.

16. Y.P. Gu, Contact Angle Measurement Techniques for Determination of Wettability, in: P. Somasundaran, A. Hubbard (Eds.), Encyclopedia of Surface and Colloid Science, Taylor & Francis, 2006.

17. L. F. M. da Silva, A. Oochsner, R. D. Adams, Handbook of Adhesion Technology, Springer-Verlag Berlin Heidelberg, 2011, ch. 4.

18. J. Drelich, Editorial, Surface Innovations 1 (2013) 1-5.

19. E. Bormashenko, Wetting of real solid surfaces - new glance on well-known problems, Colloid. Polym. Sci. 291 (2013) 339-342.

20. M. Schmitt, K. Gross, J. Grub, F. Heib, Detailed statistical contact angle analyses; "slow moving" drops on inclining silicon-oxide surfaces, J. Colloid Interface Sci. 447 (2015) 229-239.

21. H.N. Oguz, S.S. Sadhal, Effects of soluble and insoluble surfactants on the motion of drops, J. Fluid Mech. 194 (1988) 563-579.

22. A. Marmur, Line tension and the intrinsic contact angle in solid–liquid–fluid systems, J. Colloid Interface Sci. 186 (1997) 462–466.

23. A.I. Rusanov, Classification of line tension, Colloids Surf. A 156 (1999) 315–322.

24. S. Baxter, Wetting and contact-angle hysteresis, Nature 165 (1950) 198.

25. K.H. Kang, How Electrostatic Fields Change Contact Angle in Electrowetting, Langmuir 18 (2002) 10318–10322.

26. R.N. Wenzel, Surface roughness and contact angle, J. Phys. Colloid Chem. 53(1949) 1466–1467.

27. H. Kamusewitz, W. Possart, D. Paul, The relation between Young's equilibrium contact angle and the hysteresis on rough paraffin wax surfaces, Colloids and Surfaces a-Physicochemical and Engineering Aspects 156 (1999) 271-279.

28. A.B.D. Cassie, Contact angles, Discuss. Faraday Soc. 3 (1948) 11–16.

29. Y. Rotenberg, L. Boruvka, A.W. Neumann, Determination of surface tension and contact angle from the shapes of axisymmetric fluid interfaces, J. Colloid Interface Sci. 93 (1983) 169–183.

30. O.I. del Rio, A.W. Neumann, Axisymmetric drop shape analysis: computational methods for the measurement of interfacial properties from the shape and dimensions of pendant and sessile drops, J. Colloid Interface Sci. 196 (1997) 136–147.

31. A. Kalantarian, R. David, A.W. Neumann, Methodology for high accuracy contact angle measurement, Langmuir 25 (2009) 14146–14154.

32. A. Bateni, S.S. Susnar, A. Amirfazli, A.W. Neumann, Development of a new methodology to study drop shape and surface tension in electric fields, Langmuir 20 (2004) 7589–7597.

33. M. Hoorfar, A.W. Neumann, Recent progress in Axisymmetric Drop Shape Analysis (ADSA), Adv. Colloid Interface Sci. 121 (2006) 25–49.

34. L. Li, W. Kang, D. Ye, A contact angle measurement method for the droplets in EWOD-based chips, in: Proc. 2nd IEEE, Conf. Nano/Micro Eng. Molec. Sys., Bangkok, Thailand, 16th–19th January, 2007.

35. J. Goclawski, W. Urbaniak-Domagala, The method of solid–liquid contact angle measurement using the images of sessile drops with shadows on substratum, in: Proc. Memstech Lviv-Polyana, Ukraine, 23rd–26th May, 2007, pp. 135–140.

36. M. Bortolotti, M. Brugnara, C.D. Volpe, S. Siboni, Numerical models for the evaluation of the contact angle from axisymmetric drop profiles: a statistical comparison, J. Colloid Interface Sci. 336 (2009) 285–297.

37. S. Iliev, N. Pesheva, Nonaxisymmetric drop shape analysis and its application for determination of the local contact angles, J. Colloid Interface Sci. 301 (2006) 677–684.

38. S.F. Chini, V. Bertola, A. Amirfazli, A methodology to determine the adhesion forces of arbitrarily shaped drops with convex contact lines, Colloids and Surfaces A: Physicochemical and Engineering Aspects 436 (2013) 425-433.

39. A. Bateni, S.S. Susnar, A. Amirfazli, A.W. Neumann, Effect of electric fields on contact angle and surface tension of drops, Colloids Surf. A 219 (2003) 215–231.

40. S. Schuetter, T. Shedd, K. Doxtator, G. Nellis, C. Van Peski, A. Grenville, S.H. Lin, D.C. Owe-Yang, Measurements of the dynamic contact angle for conditions relevant to immersion lithography, J. Microlithogr. Microfab. Microsyst. 5 (2006) 023002.

41. S.F. Chini, A. Amirfazli, A method for measuring contact angle of asymmetric and symmetric drops, Colloids and Surfaces A: Physicochemical and Engineering Aspects, 388 (2011) 29-37.

42. A.F. Stalder, G. Kulik, D. Sage, L. Barbieri, P. Hoffmann, A snake-based approach to accurate determination of both contact points and contact angles, Colloids Surf. A 286 (2006) 92–103.

43. C. Xu, J.L. Prince, Snakes, shapes, and gradient vector flow, IEEE Trans. Image Process. 7 (March) (1998) 359–369.

44. D. Biolè, V. Bertola, A goniometric mask to measure contact angles from digital images of liquid drops, Colloids Surfaces A Physicochem. Eng. Asp. 467 (2015) 149–156.

45. D. Biolè, V. Bertola, The fuzzy interface of a drop, Comput. Vis. Sci. 17 (2015) 19-32.

46. M. Schmitt, F. Heib, High-precision drop shape analysis on inclining flat surfaces: Introduction and comparison of this special method with commercial contact angle analysis J. Chem. Phys. 139 (2013) 134201.

47. V. Bertola, M. Wang, Apparent dynamic contact angle measurements for dilute polymer solution drops impacting on a hydrophobic surface, Colloids and Surfaces A: Physicochemical and Engineering Aspects 481 (2015), 600-608.

48. V. Bertola, Effect of polymer additives on the apparent dynamic contact angle of impacting drops, Colloids and Surfaces A: Physicochemical and Engineering Aspects 363 (2010) 135-140.

49. M. Versluis, High-speed imaging in fluids, Exp. Fluids, 54 (2013) 1-35.

50. W. Burger and M. J. Burge, Digital Image Processing, 1st ed. Springer, 2008.

51. R. C. Gonzales and R. E. Woods, Digital Image Processing, Third Edit. Prentice Hall, 2008.

52. M. Nixon and A. S. Aguado, Feature Extraction & Image Processing for Computer Vision, Elsevier Science, 2012.

53. J. Canny, A computational approach to edge detection, IEEE Trans. Pattern Anal. Mach. Intell., 8 (1986) 679–698.

54. V. Bertola, Dynamic wetting of dilute polymer solutions : The case of impacting droplets, Adv. Colloid Interface Sci. 193–194, (2013) 1–11.

55. N. P. Cheremisinoff, Handbook of Engineering Polymeric Solutions. New York: Marcel Dekker, 1997.

56. V. N. Kalashnikov and A. N. Askarov, Relaxation time of elastic stresses in liquids with small additions of soluble polymers of high molecular weights, J. Eng. Phys. 57, (1989) 874–878.

57. http://www.ualberta.ca/~chini/index.html.

58. T. Lindeberg, Edge detection and ridge detection with automatic scale selection, Proc. CVPR IEEE Comput. Soc. Conf. Comput. Vis. Pattern Recognit., pp. 465–470, 1996.

59. T. Lindeberg, Scale-space, Encyclopedia of Computer Science and Engineering, 4 (2009), 2495–2504.
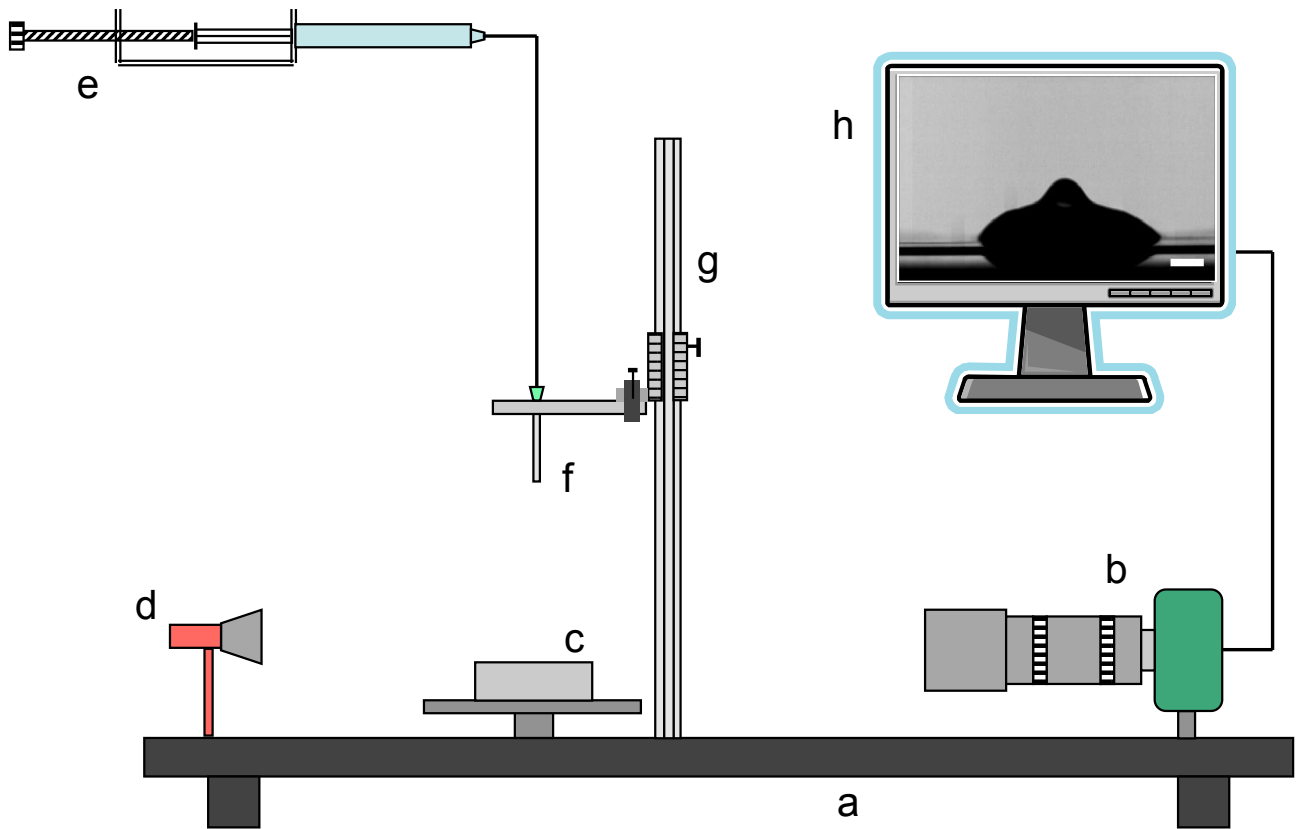
Figure 1. Schematic of the experimental setup: (a) optical breadboard, (b) Phantom V9.1 high–speed camera and zoom lens, (c) PTFE substrate, (d) LED light source (e) screw driven syringe pump, (f) hypodermic needle, (g) Vernier height gauge, (h) data acquisition system.

| | | | |
|---|---|---|---|
| t = 0 ms | t = 1 ms | t = 3 ms | t = 5 ms |
| t = 10 ms | t = 15 ms | t = 20 ms | t = 25 ms |
| t = 30 ms | t = 35 ms | t = 40 ms | t = 45 ms |

Figure 2. Example of side views of a liquid drop during impact after background subtraction (We = 48).
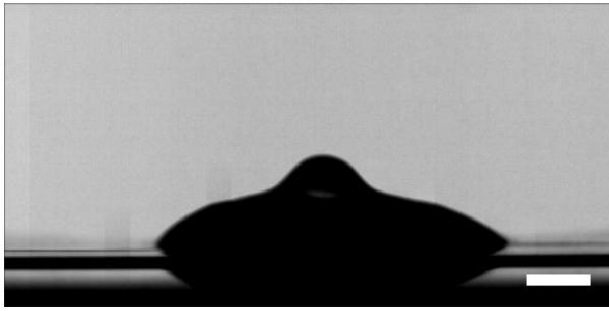
[a] $t = 10$ ms
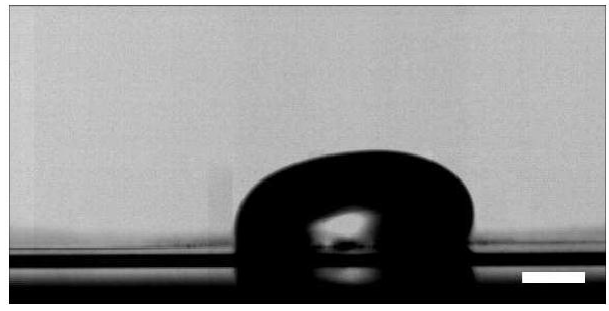


[b] $t = 25$ ms
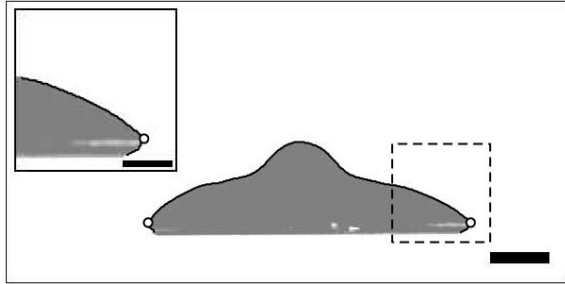


[c] $t = 10$ ms
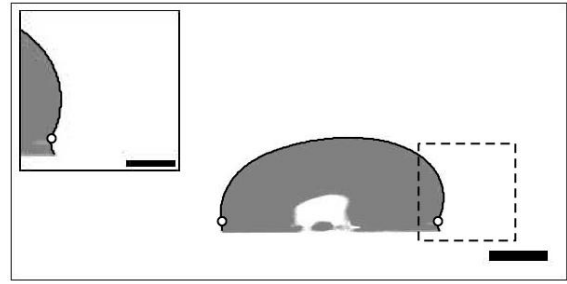


[d] $t = 25$ ms

Figure 3: side views of a polymer drop captured at different impact times for We=48: [a-b] original frames, [c-d] pre-processed frames (i.e. background subtraction, interface detection by Canny edge detector); insets show the right contact point region magnified of a factor of 2, length bars correspond to 1 mm for images, and 0.5 mm for insets
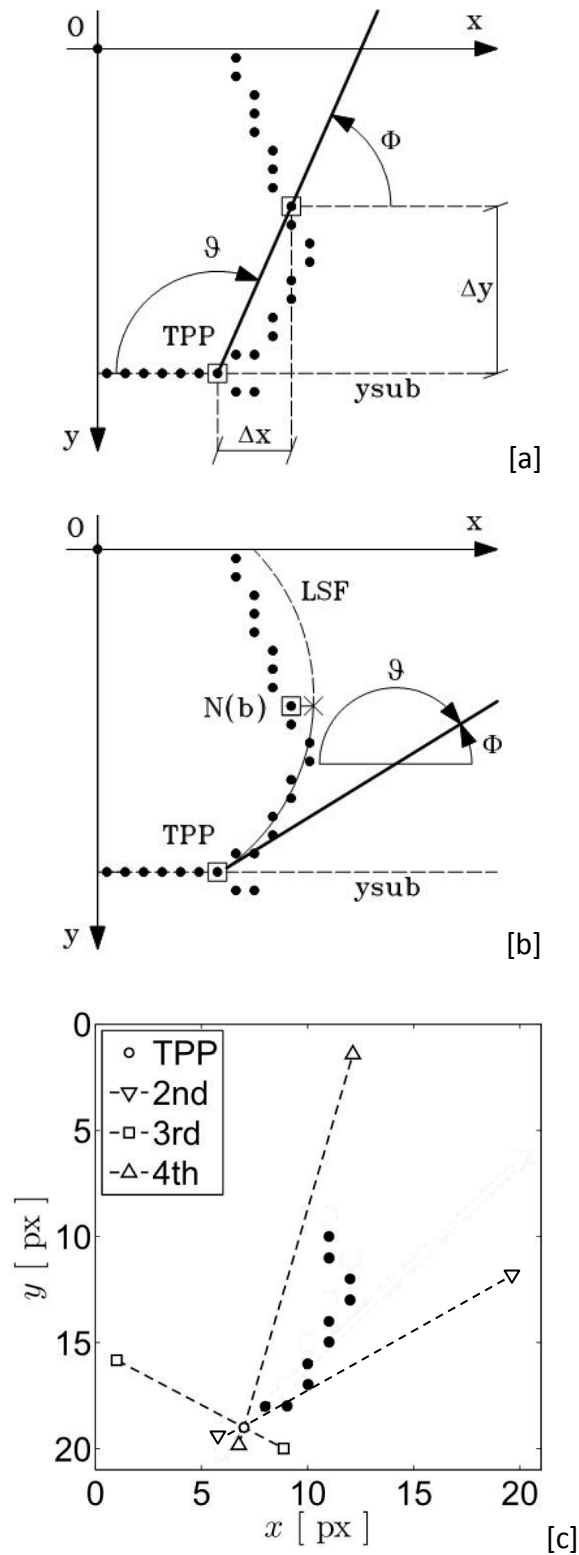
Figure 4. Contact angle measurement on a discretised drop edge by local fitting: [a] secant method; [b] polynomial edge fitting method ($2^{nd}$ order, continuous line between the triple point and the asterisk); [c] tangent lines to three polynomial functions having different order fitting the same group of discrete points and interpolating the three phase point (TPP).
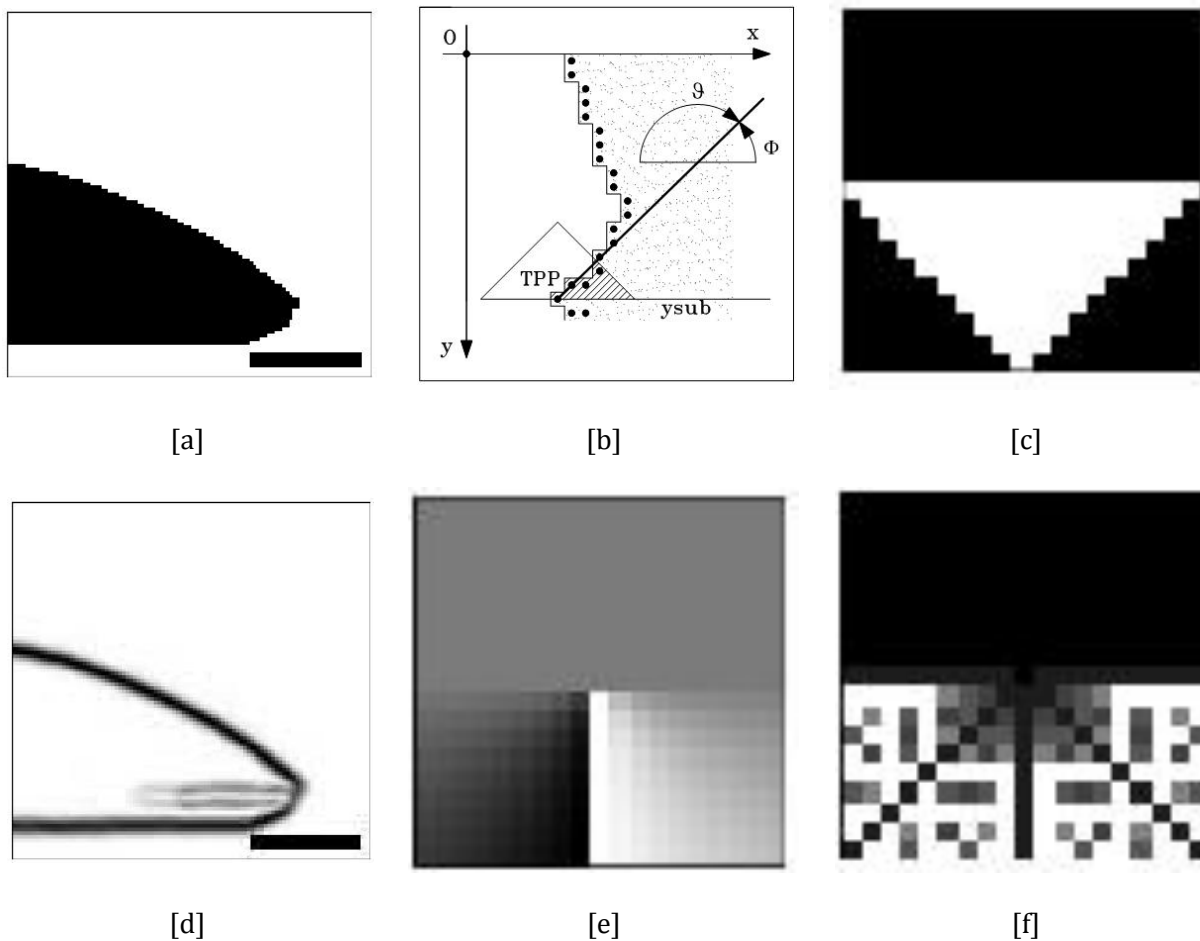
[a]  [b]  [c]

[d]  [e]  [f]

Figure 5. Schematic description of the local contour analysis method ([a]-[c]) and of the intensity gradient analysis method ([d]-[f]). [a] example of binary input image; [b] detail of the reference geometric construction; [c] convolution mask; [d] intensity gradient of the sample drop image; [e] directional angle mask; [e] weighing mask for the probability distribution of the angle.
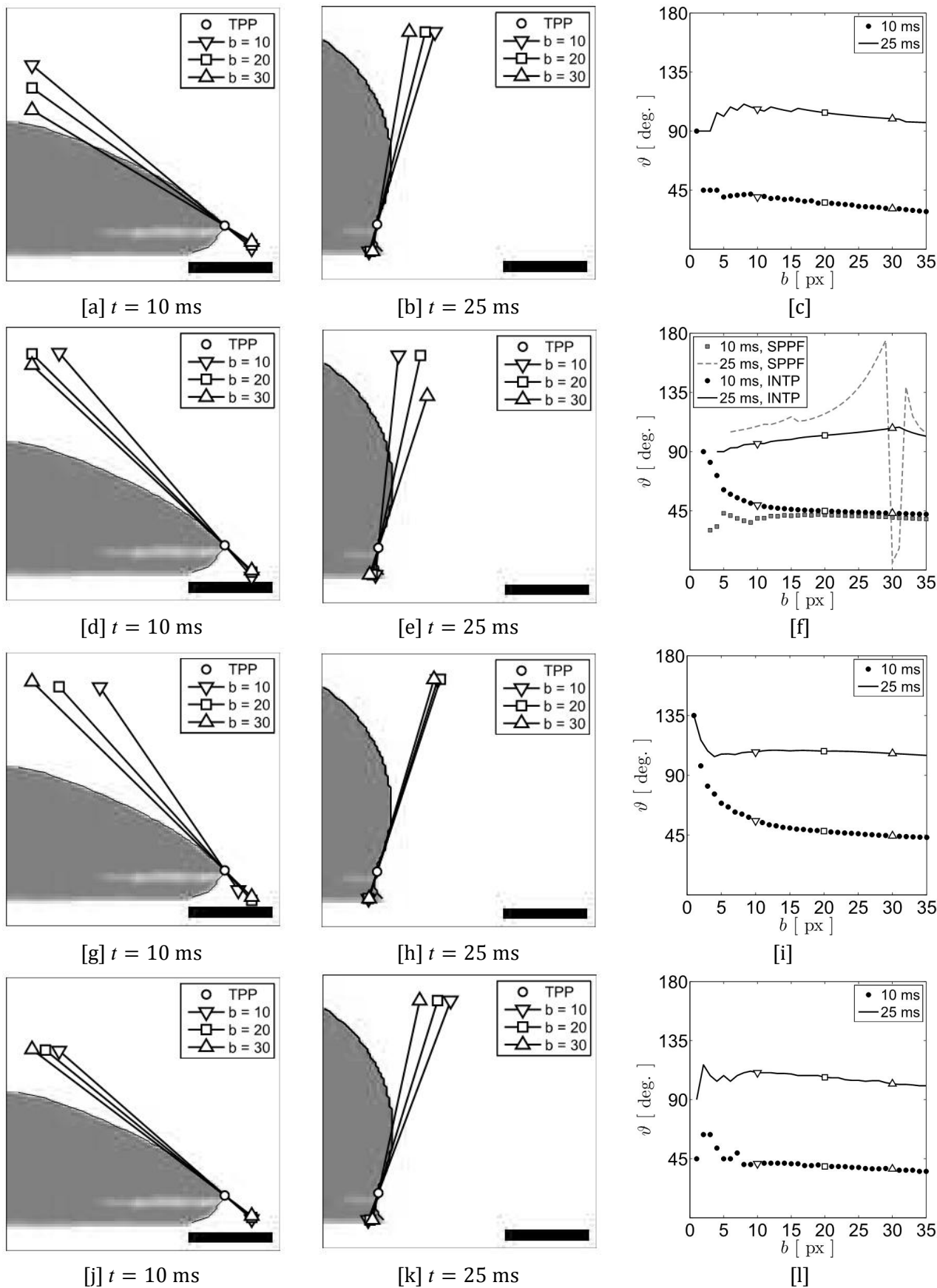
Figure 6. Contact angle measurement of single test frames using the secant method [a-c], polynomial edge fitting [d-f], local contour analysis [g-i], and intensity gradient statistic [j-l], for different values of the method parameter b (see text for definition). In frames [d-e], tangent lines were obtained using a polynomial interpolating the contact point TPP (INTP data set in panel [f]).
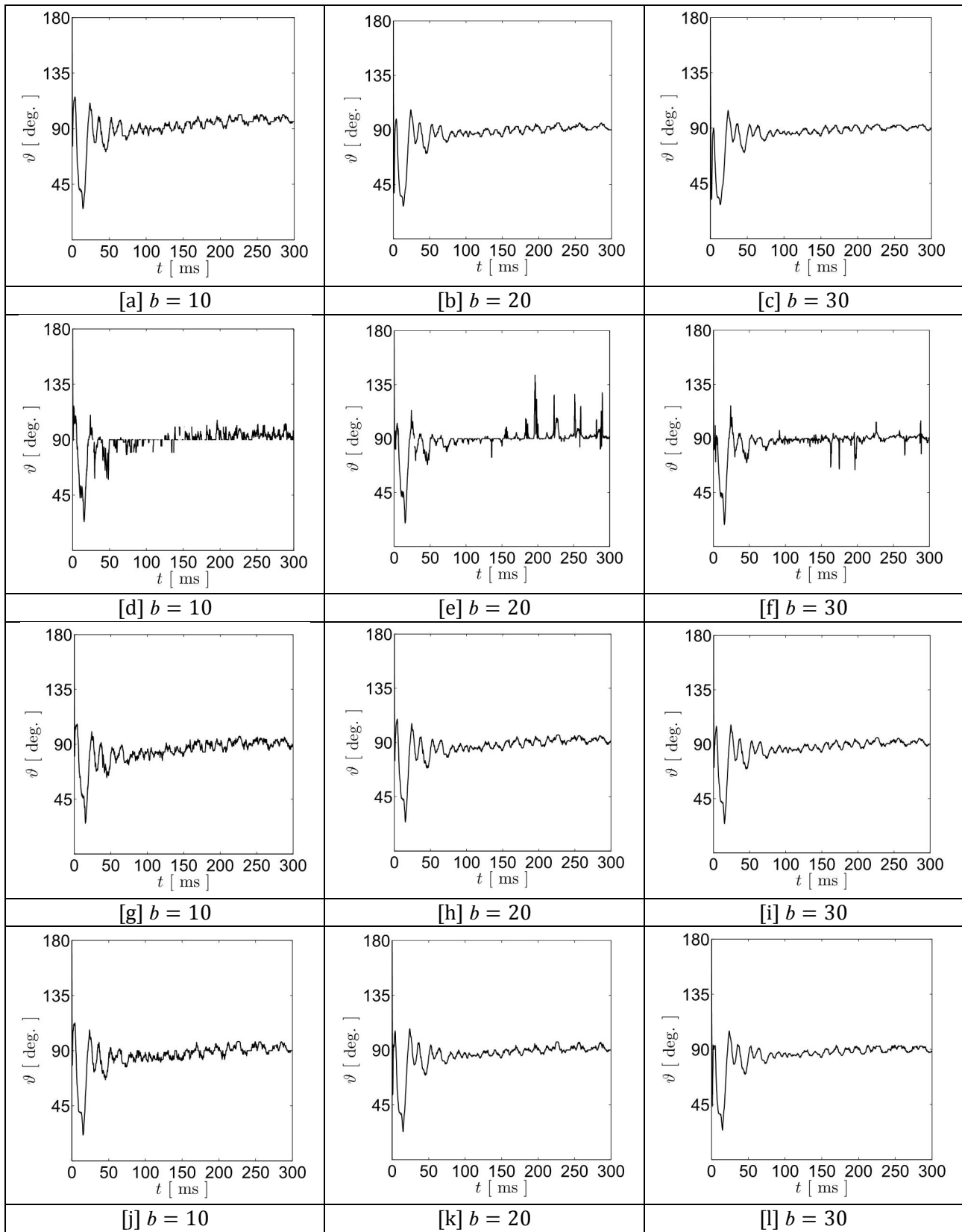
23

Figure 7. Dynamic contact angle measurements obtained using the secant method [a-c], polynomial edge fitting [d-f], local contour analysis [g-i], and intensity gradient statistic [j-l], for different values of the method parameter b (see text for definition). In frames [d-f], contact angles were measured using a polynomial fit interpolating the contact point TPP.